Using bio-based $CaCO_3$ functionalized sediment to simultaneously remove algae and COD through adsorption and sedimentation in water source reservoirs

Supplementary Information

Yifan Du[a,b] Jinbo Zhao[a,b] Qingping Wang[a] Jiacheng Feng[a] Jinyi Qin[a,b,*]

Ming Su[b,c,*]

[a] School of Civil Engineering, Chang'an University, Xi'an 710064, China.

[b] Key Laboratory of Environmental Aquatic Chemistry, State Key Laboratory of Regional Environment and Sustainability, Research Center for Eco-Environmental Sciences, Chinese Academy of Sciences, Beijing 100085, China.

[c] University of Chinese Academy of Sciences, Beijing 100049, China.

[*] Corresponding to: Jinyi Qin (jinyi.qin@chd.edu.cn), Ming Su (mingsu@rcees.ac.cn)

Figures and/or tables are provided below as the supplementary evidences to the main text.

Table of contents

Supplementary methods

Langmuir equation (Veith and Sposito, 1977)

The equation for the pseudo-first-order kinetic model is (Eq. S1 and S2):

$$\ln(q_{e,cal} - q_t) = \ln q_e - k_1 t \text{ (S1)}$$

$$\ln(q_e - q_t) = \ln q_e - k_1 t \text{ (S2)}$$

The equation for the pseudo-second-order kinetic model is (Eq. S3):

$$\frac{t}{q_t} = \frac{1}{k_2 q_e^2} + \frac{t}{q_e} \text{ (S3)}$$

$$q_e = \frac{C_i - C_f}{S} \text{ (S4)}$$

$$q_t = \frac{C_i - C_t}{S} \text{ (S5)}$$

Where, q_e (μg g^{-1}) (Almomani and Bhosale, 2021) is the experimental equilibrium adsorption capacity of the adsorbent; q_t (μg g^{-1}) (Almomani and Bhosale, 2021) is the equilibrium adsorption amount of the adsorbent at time t (min); $q_{e,cal}$ and q_e (μg g^{-1}) are the theoretical and actual equilibrium adsorption amounts, respectively; k_1 (min^{-1}) is the pseudo-first-order kinetic model constant, k_2 (g (mg min) $^{-1}$) is the pseudo-second-order kinetic model constant.

The equilibrium adsorption data were analyzed using both Langmuir (Eq. S6) and Freundlich (Eq. S8) isotherm models (Almomani and Bhosale, 2021) to characterize the adsorption process.

$$q_e = \frac{q_m K_L C_e}{1 + K_L C_e} \text{ (S6)}$$

$$R_L = \frac{1}{1 + K_L C_e} \text{ (S7)}$$

$$q_e = K_F (C_e)^{\frac{1}{n}} \text{ (S8)}$$

Where, q_m is the maximum Chl-a concentration adsorbed on unit mass of micro-nano $CaCO_3$ (μg g^{-1}), K_L is the Langmuir adsorption constant (μg L^{-1}); R_L is the separation coefficient (Eq. S6); K_F is the Freundlich adsorption constant (μg g^{-1}) (L $\mu g^{-1})^{1/n}$; C_e is the adsorption equilibrium

solution concentration (μg L^{-1}), and $1/n$ is the adsorption intensity coefficient (Huang et al., 2020). A value of $1/n$ in the range $0 < 1/n < 1$ indicates favorable adsorption with high affinity, while $1/n > 1$ suggests poor adsorption and low surface affinity. The closer $1/n$ is to 0, the stronger the adsorption intensity; conversely, larger $1/n$ values reflect increased surface heterogeneity and weaker adsorption.

A dimensionless separation factor (R_L) is introduced from the Langmuir equation to evaluate whether the adsorption of bio-$CaCO_3$ to algae is a favorable spontaneous reaction (Eq. S9).

$$R_L = \frac{1}{(1+K_L C_0)} \quad \text{(S9)}$$

When $R_L > 1$, it is unfavorable for the material's adsorption; when $R_L = 1$, the material's adsorption is linear; when R_L=0, the material's adsorption is irreversible; when $0 < R_L < 1$, it indicates that the material's adsorption process is favorable. In the range of 0~1, the larger the value, the more favorable it is for the material to remove pollutants.

Young's equation (Novak and Brune, 1985)

$$G_{h_0}^{AB} = 2\left[\sqrt{\gamma_\omega^+}\left(\sqrt{\gamma_f^-} + \sqrt{\gamma_m^-} - \sqrt{\gamma_\omega^-}\right) + \sqrt{\gamma_\omega^-}\left(\sqrt{\gamma_f^+} + \sqrt{\gamma_m^+} - \sqrt{\gamma_\omega^+}\right) - \sqrt{\gamma_f^-\gamma_m^+} - \sqrt{\gamma_f^+\gamma_m^-}\right]$$

$$G_{h_0}^{LW} = -2\left(\sqrt{\gamma_m^{LW}} + \sqrt{\gamma_\omega^{LW}}\right)\left(\sqrt{\gamma_f^{LW}} + \sqrt{\gamma_\omega^{LW}}\right)$$

(S10)

$$\Delta G_{h_0}^{EL} = \frac{\varepsilon_r \varepsilon_0 \kappa}{2}(\xi_m^2 + \xi_f^2)[(1 - \cot h(\kappa h_0) + \frac{2\xi_m \xi_f}{\xi_m^2 + \xi_f^2}(\csc h(\kappa h_0))]$$

(S11)

Where $G_{h_0}^{AB}$, $G_{h_0}^{LW}$ and $\Delta G_{h_0}^{EL}$ is the individual interaction per unit area at h_0, γ^- and γ^+ are the electron donor and electron acceptor components of surface tension, respectively, and γ^{LW} is the Lifshitz–van der Waals component. The subscript w denotes the aqueous medium, and θ is the contact angle ζm and ζp (mV) are the membrane and particle zeta potentials.

$$\frac{(1 + \cos\varphi)}{2}\gamma_l^{\mathrm{Tol}} = \sqrt{\gamma_l^{\mathrm{LW}}}\sqrt{\gamma_s^{\mathrm{LW}}} + \sqrt{\gamma_l^-}\sqrt{\gamma_s^+} + \sqrt{\gamma_l^+}\sqrt{\gamma_s^-}$$

$$\gamma^{\mathrm{Tol}} = \gamma^{\mathrm{LW}} + \gamma^{\mathrm{AB}}$$

(S12)

$\gamma^{AB} = 2\sqrt{\gamma_l^-\gamma_s^+}$ (S13)

$\kappa = \sqrt{\frac{e^2 \sum n_i z_i}{\varepsilon \varepsilon_0 \kappa T}}$ (S14)

Where e is the elementary charge, i is the number concentration of the ions in the dispersed solution, Z_i is the valence of the ions, k is the Boltzmann constant, and T is the absolute tempera-

ture, ($\varepsilon_0 = 8.85 \times 10^{-12} \mathrm{CV}^{-1} m^{-1}$) (Oss, 1993) is the dielectric constant of vacuum, ($\varepsilon = 78.5$) is the dielectric constant of water.

DFT Calculations

All density functional theory (DFT) calculations were performed using the Vienna Ab initio Simulation Package (VASP) (Kresse and Furthmüller, 1996). The exchange–correlation interactions were treated using the generalized gradient approximation (GGA) with the Perdew–Burke–Ernzerhof (PBE) functional (Perdew et al., 1996). To account for dispersion forces, Grimme's DFT-D3 empirical correction was applied (Grimme et al., 2010). A vacuum slab of approximately 15 Å was introduced perpendicular to the surface to eliminate interactions between periodic images.

A plane-wave cutoff energy of 450 eV was used. Brillouin zone sampling was conducted using a Γ-centered Monkhorst–Pack k-point mesh of 3 × 3 × 1 (Monkhorst and Pack, 1976). Full geometric optimizations were carried out until the residual force on each atom was less than 0.02 eV/Å and the total energy convergence threshold was set to 10^{-5} eV.

The adsorption energy (ΔE) was calculated according to Eq. S15:

$$\Delta E = E_{ads/surf} - E_{\text{surf}} - E_{\text{ads}} \quad \text{(S15)}$$

where $E_{\text{ads/surf}}$ is the total energy of the adsorbate–substrate system, E_{surf} is the energy of the clean surface, and E_{ads} is the energy of the isolated adsorbate in vacuum.

Response surface design (Anderson-Cook et al., 2009)

A Box Behnken Design (BBD) was employed to optimize the algae removal process with minimal experimental runs. Three key factors—mass fraction of nano-$CaCO_3$ (A), the molar ratio of Ca^{2+} to CO_3^{2-} (B), and reaction time (C)—were selected as independent variables. The removal efficiencies of Chl-a (Y_1) and COD (Y_2) served as response variables. A total of 17 experimental runs were determined (S16). The independent variables were coded as X_1, X_2 and X_3 (S17), and a second-order polynomial model was used to fit the response data.

$$N = 2^k + 2k + C_0 \quad \text{(S16)}$$

Where N is the number of experiments; k is the number of experimental factors,$k = 3$; C_0 is the number of repeated experiments at the center point, $C_0 = 3$.

$$Z_i = \frac{X_i - X_0}{\Delta X} \quad \text{(S17)}$$

Where: Z_i is the dimensionless coded value of the i-th influencing factor; is the actual value of the i-th influencing factor; X_0 is the actual value of X_i at the center point; ΔX is the difference between the actual value of the high level and the actual value of the center level of each influencing factor.

The quadratic polynomial model (S18) was applied to predict system behavior and identify optimal conditions:

$$Y = \beta_0 + \sum_{i=1}^{K} \beta_i X_i + \sum_{i=1}^{k-1} \sum_{j=i+1}^{k} \beta_{ij} X_i X_j + \sum_{i=1}^{k} \beta_{ij} X_i^2 \quad \text{(S18)}$$

where: Y represents the predicted response (removal efficiency), β_0 is the constant coefficient, β_i are linear effect coefficients, β_{ij} are interaction effect coefficients, β_{ii} are quadratic effect coefficients, X_i and X_j denote coded values of independent variables.

Supplementary figures

Fig. S1

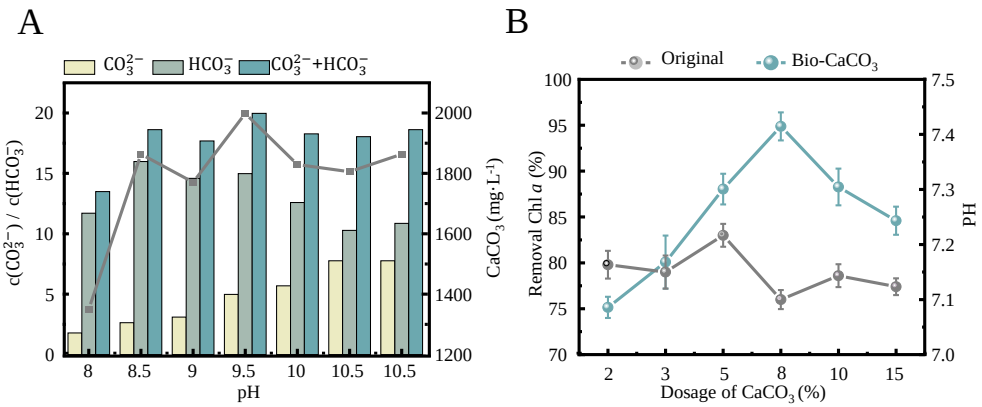

Fig. S1: Variations in CO_3^{2-}, HCO_3^-, and total carbonate concentration (CO_3^{2-} + HCO_3^-) under different pH conditions. As pH increased, the CO_3^{2-}/HCO_3^- ratio rose markedly, indicating enhanced conversion of HCO_3^- to CO_3^{2-}, which coincided with elevated $CaCO_3$ concentrations (A). Effect of $CaCO_3$ dosage on Chl-a removal and pH. Bio-$CaCO_3$ exhibited significantly higher removal efficiency than original $CaCO_3$, with a peak at 8% dosage. The pH values also slightly increased with Bio-$CaCO_3$ addition (B).

Fig. S2

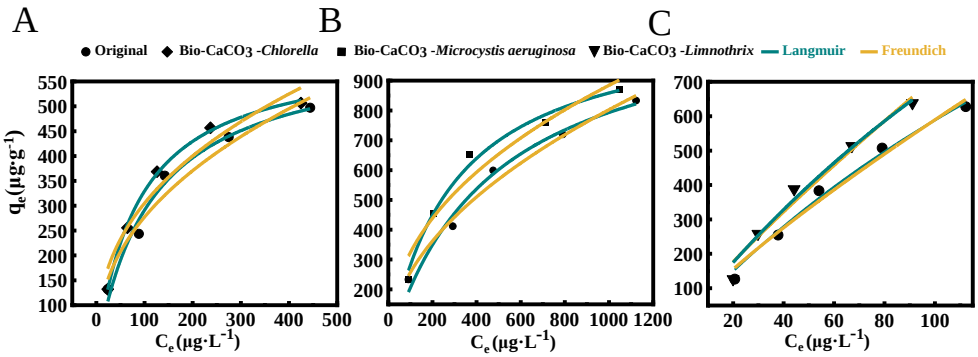

Fig. S2: Adsorption isotherm fitting of three algal species onto unmodified and Bio-$CaCO_3$-modified materials using Langmuir and Freundlich models. (A) *Chlorella*, (B) *Microcystis aeruginosa*, and (C) *Limnothrix*. Symbols represent experimental data for original and Bio-$CaCO_3$-treated samples, while solid lines correspond to model fitting curves. The Langmuir model (blue) describes monolayer adsorption on homogeneous surfaces, whereas the Freundlich model (orange) reflects multilayer adsorption on heterogeneous surfaces.

Fig. S3

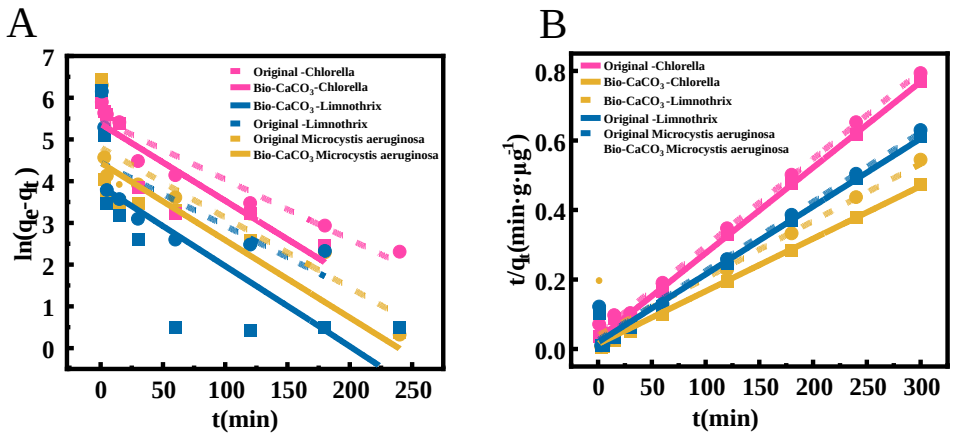

Fig. S3: Kinetic modeling of algal adsorption onto unmodified and Bio-$CaCO_3$-modified materials. (A) Pseudo-second-order model fitting; (B) Pseudo-first-order model fitting. Symbols represent experimental data for three algal species (*Chlorella*, *Limnothrix*, and *Microcystis aeruginosa*) under original and Bio-$CaCO_3$-modified conditions. Solid and dashed lines denote corresponding model fittings. The pseudo-second-order model (A) generally provided a better fit to the experimental data, indicating chemisorption as the dominant rate-controlling mechanism.

Fig. S4

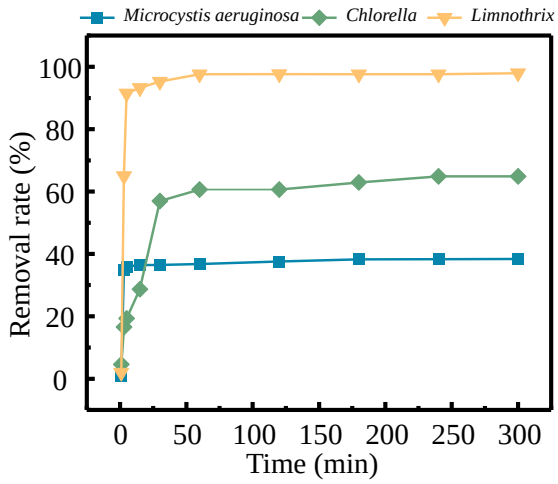

Fig. S4: Removal rates of *Chlorella*, *Microcystis aeruginosa*, and *Limnothrix* by modified sediment over time (0–300 min). All three algal species exhibited a rapid increase in removal efficiency during the initial phase, eventually reaching adsorption saturation. *Limnothrix* showed the highest removal rate, followed by *Chlorella* and *Microcystis aeruginosa*.

Fig. S5

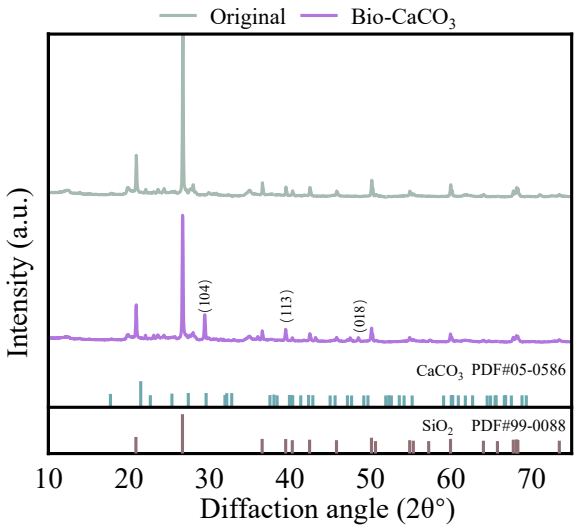

Fig. S5: X-ray diffraction (XRD) patterns of original and biologically modified $CaCO_3$ (Bio-$CaCO_3$). The diffraction peaks corresponding to $CaCO_3$ and SiO_2 are identified. Compared with the original sample, Bio-$CaCO_3$ exhibits enhanced peak intensity and crystallinity of $CaCO_3$, indicating improved mineralization and structural ordering induced by biological modification.

Fig. S6

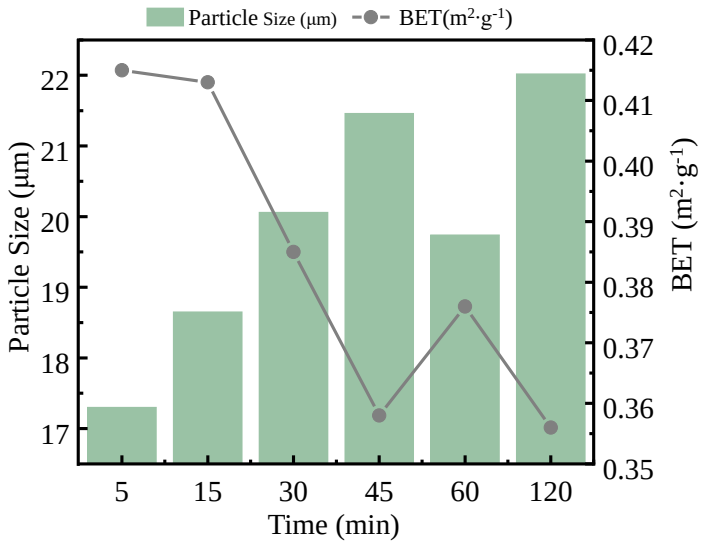

Fig. S6: Changes in particle size and BET surface area of $CaCO_3$ under different reaction times. Particle size increased with prolonged reaction, while BET surface area generally showed a decreasing trend, indicating structural densification over time.

Fig. S7

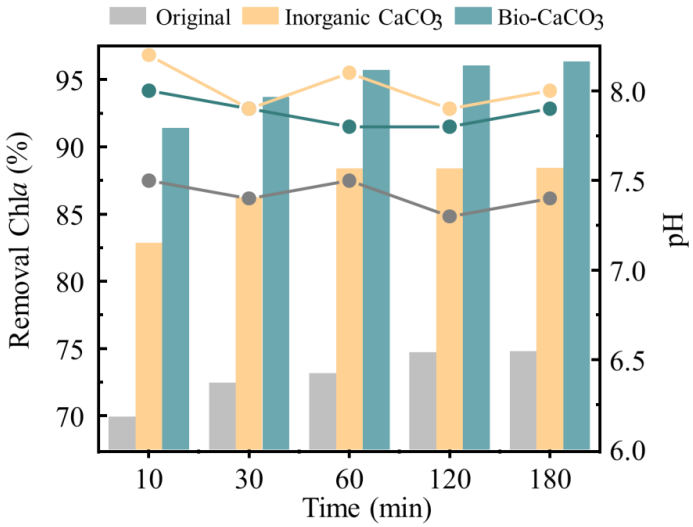

Fig. S7: Chl-a removal efficiency and pH variation over time under three sediment treatments: Original sediment, Inorganic $CaCO_3$, and Bio-$CaCO_3$. Bio-$CaCO_3$ exhibited the highest removal efficiency, peaking at over 95% at 60 min, while maintaining a pH closest to that of natural water.

137 **Fig. S8**

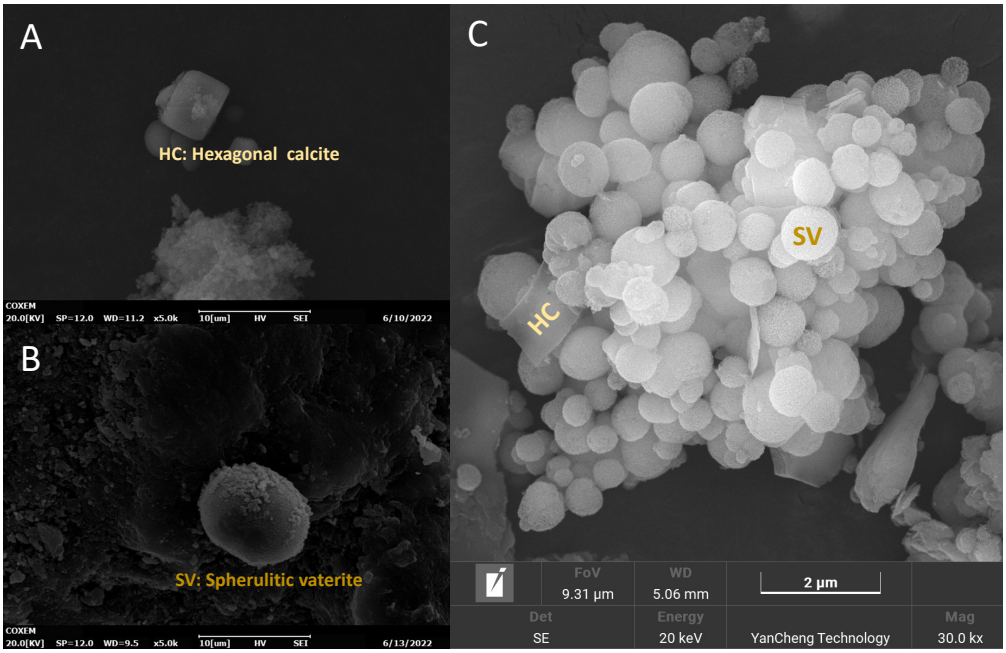

Fig. S8: SEM images illustrating the morphological distinction between $CaCO_3$ obtained via conventional chemical synthesis and biogenic formation, underscoring the *in-situ* structural adaptability of bio-$CaCO_3$ within sediments. (A) Chemically synthesized $CaCO_3$ presenting well-faceted hexagonal calcite (HC). (B) Biogenic $CaCO_3$ showing spherulitic vaterite (SV) aggregates. (C) Bio-$CaCO_3$ from this study, predominantly composed of amorphous micro–nanospheres with localized development of hexagonal calcite at particle peripheries, indicating *in-situ* secondary growth from amorphous precursors while preserving a high-reactivity, amorphous-rich framework.

Fig. S9

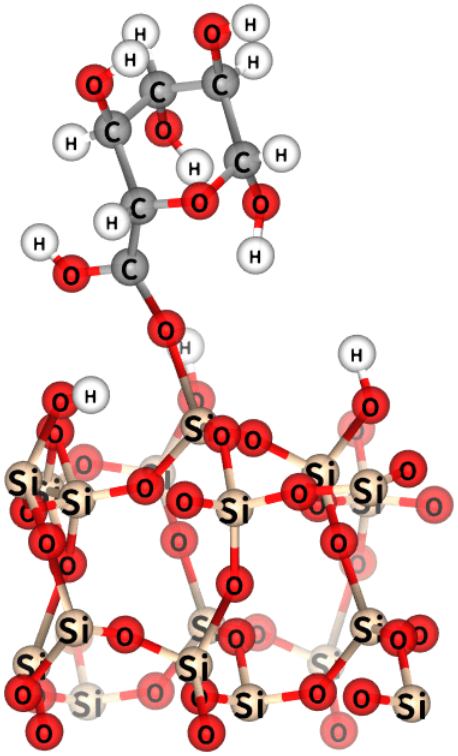

Fig. S9: A static image of an animated character (Supplementary File: `FigS9.gif`). Time-resolved molecular dynamics snapshot showing the adsorption configuration of glucuronic acid on an unmodified silanol-rich silica surface. Silicon atoms are shown in beige, oxygen in red, carbon in grey, and hydrogen in white. The molecular conformation illustrates hydrogen bonding interactions between the hydroxyl/carboxyl groups of glucuronic acid and surface silanol groups, corresponding to the structural model used for bond length and bond angle trajectory analysis in Fig. S11A–D.

Fig. S10

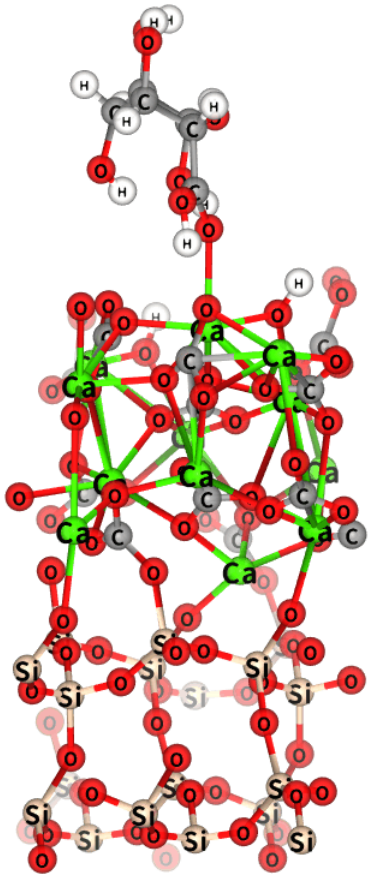

Fig. S10: A static image of an animated character (Supplementary File: `FigS10.gif`). Atomic configuration from DFT molecular dynamics simulation showing the interaction between glucuronic acid and the bio-$CaCO_3$–modified silica surface. Gray, red, white, beige, black, and green spheres represent C, O, H, Si, Ca–C carbonate groups, and Ca atoms, respectively. Ca atoms form coordination bonds with surface oxygen atoms and bridge carbonate groups to the silica substrate, illustrating the Ca–O–Si linkage and multi-point anchoring mechanism at the bio-$CaCO_3$–modified interface. This structural model corresponds to that used for bond length and bond angle trajectory analyses shown in Fig. S11E–H.

Fig. S11

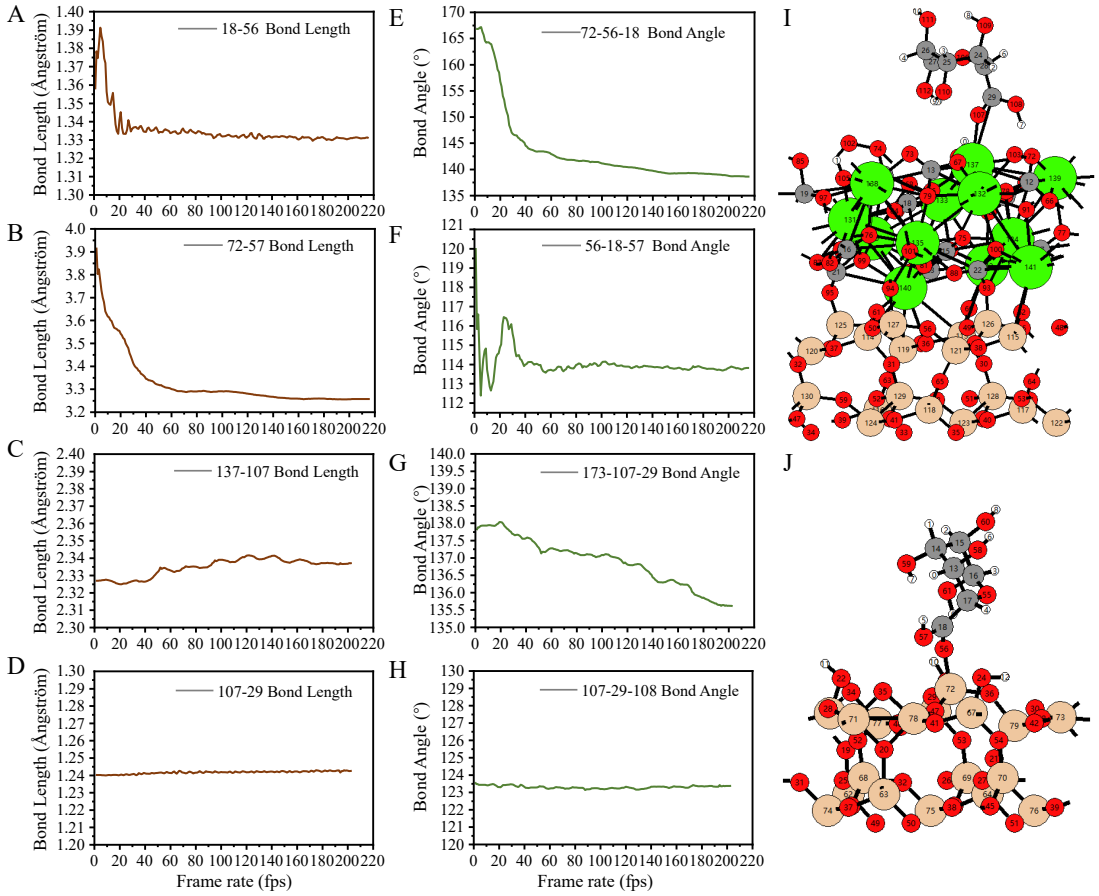

Fig. S11: Time-resolved trajectories of bond length and bond angle variations derived from DFT molecular dynamics simulations of glucuronic acid interacting with sediment surfaces. (A–D) Unmodified silanol-rich silica surface (corresponding to the atomic configuration in panel J): (A) C–O (18–56) bond length variation, (B) O–H · · · O (72–57) hydrogen bond distance, (C) Ca–O (137–107) coordination distance, and (D) C–O (107–29) bond length. (E–H) Bio-$CaCO_3$–modified silica surface (corresponding to the atomic configuration in panel I): (E) O–C–O (72–56–18) bond angle variation, (F) Si–O–Si (56–18–57) bond angle evolution, (G) O–Ca–O (173–107–29) bond angle variation, and (H) C–O–Si (107–29–108) bond angle variation. (I–J) Atomistic configurations showing labeled atoms used for trajectory extraction: (I) bio-$CaCO_3$–modified silica surface, (J) unmodified silica surface.

Supplementary tables

Table S1

Ingredients	Content (%)	Unit
pH	7.59±0.1	—
TDS	283.88±0.5	mg L^{-1}
TH	106.94±0.5	mg L^{-1}($CaCO_3$)
EC	62.17±1.5	µS cm^{-1}
TP	20±0.3	µg L^{-1}
TN	3.2±0.04	mg L^{-1}
$COD_{(Mn)}$	3.0±0.2	mg L^{-1}
K^+	0.91±0.03	mg L^{-1}
Na^+	9.55±0.05	mg L^{-1}
Ca^{2+}	83.53±0.2	mg L^{-1}
Mg^{2+}	25.96±0.1	mg L^{-1}
Cl^-	12.99±0.03	mg L^{-1}
SO_4^{2-}	12.27±0.02	mg L^{-1}
HCO_3^-	201.73±0.3	mg L^{-1}

Table S1: The measured parameters include pH, total dissolved solids (TDS), total hardness (as $CaCO_3$), electrical conductivity (EC), and major nutrient and ion concentrations. These values represent typical background conditions of a clean drinking water reservoir. Data are expressed as mean ± standard deviation (n = 3).

Table S2

Ingredients	Content (%)
SiO_2	68.72
Al_2O_3	19.56
Fe_2O_3	4.19
MgO	1.01
CaO	1.12
Na_2O	0.75
K_2O	2.9
MnO	0.06
P_2O_5	0.22
TiO_2	0.86
SO_3	0.53
Cl	0.05
Zn	0.01
Sr	0.01

Table S2: Chemical composition of the sediment sample based on X-ray fluorescence (XRF) analysis. SiO_2 and Al_2O_3 were the dominant components, followed by Fe_2O_3, K_2O, and minor amounts of CaO, MgO, and other trace elements.

Table S3

Detection liquid	γ^{LW}	γ^{+}	γ^{-}	γ^{AB}	γ^{Tol}
Ultrapure water	21.8	25.5	25.5	51.0	72.8
Formamide	39.0	2.28	39.6	19.0	58
Diiodomethane	50.8	0.0	0.0	0.0	50.8

Table S3: Surface tension (mJ m^{-2}) of the probe liquid, according to (Oss, 1995, 1995).

Table S4

Factor	-1	0	1
A: Added fraction of $CaCO_3$ (%)	2	8	14
B: Residual free Ca^{2+} (%)	0	50	100
C: Time of reaction (min)	10	60	110

Table S4: Codes and levels of experimental factors for BBD

Table S5

Time (min)	*Chlorella vulgaris* (µg L^{-1})		*Microcystis aeruginosa* (µg L^{-1})		*Limnothrix* sp. (µg L^{-1})	
	Control	Experimental	Control	Experimental	Control	Experimental
1	1139.4	1145.02	3245.2	3273.1	970.3	980.38
3	1142.7	1001.16	3252.6	2147.44	954.8	350.36
5	1135.3	968.22	3238.9	2113.0	940.1	85.24
15	1137.9	855.88	3248.7	2097.76	910.2	67.86
30	1140.1	516.42	3240.3	2095.94	885.4	47.4
60	1132.6	472.26	3235.8	2086.22	860.5	23.7
120	1139.0	472.26	3242.1	2059.28	880.2	23.54
180	1128.0	444.84	3238.0	2035.9	900.7	23.7
240	1133.8	421.3	3244.5	2035.58	920.9	23.7
300	1130.0	421.3	3239.9	2032.66	945.6	20.46

Table S5: Time-course of Chl-a concentrations in centrifugation-only controls & Bio-$CaCO_3$-treated groups for three algal species.

147 ## Table S6

		Equilibrium parameters of adsorption			Adsorption	kinetics
Category		Langmuir	Freundlich		First-order kinetic	Secondary-orderki-netic
		K_L ($L\ \mu g^{-1}$)	1/n	K_F ($\mu g\ g^{-1}$) ($L\ \mu g^{-1}$)1/n	K_1 (min^{-1})	$K_2 \times 10^{-6}$ ($g\ (\mu g\ min)^{-1}$)
Chlorella	Original	0.009	0.418	40.378	0.014	6.35
	Bio-$CaCO_3$	0.011	0.391	50.331	0.0184	6.05
Microcystis aerugi-nosa	Original	0.002	0.495	26.24	0.0168	2.689
	Bio-$CaCO_3$	0.003	0.436	43.36	0.0185	2.280
Limnothrix	Original	0.004	0.841	12.24	0.0152	3.960
	Bio-$CaCO_3$	0.003	0.964	13.29	0.0191	3.841

Table S6: Equilibrium and Adsorption kinetics of algae on biomodified sediments parameters

148 ## Table S7

	Surface free energy parameters (mJ m^{-2})			Aii ($\times 10^{-21}$ J)		
	γ^+	γ^-	γ^{LW}		A132 ($\times 10^{-21}$ J)	Surface energy(mN m^{-1})
Modified Sediments	0.6	31.61	39.99	57.58	5.41	48.69
Algae organisms	0.21	56.54	48.18	69.37	5.12	55.07
Unmodified Sediments	0.08	34.72	38.88	55.99		42.21
MilliQ water	25.5	25.5	21.8	31.39		

Table S7: Surface energy characteristics and calculated Hamaker constants (A_{132}) for assessing sediment–algae interactions.

Table S8

Surface/ Solution	Zeta potential	Contact angle (°)			Surface tension values (mJ m^{-2})			ΔGAB
	(mV)	θ_W	θ_F	θ_D	γ_{LW}	γ^+	γ^-	(mJ m^{-2})
Modified Sediments	-9.65	45°66’	34°62’	39°24’	39.99	0.60	31.61	31.282
Organisms	-5.78	7°2’	9°2’	18°6’	48.18	0.21	56.54	26.373
Unmodified Sediments	-14.6	49°46’	44°76’	42°26’	38.88	0.08	34.72	

Table S8: Contact angle of $CaCO_3$ with algae cells and surface thermodynamic parameters

Table S9

Std	Run	Factor 1 Mass fraction of $CaCO_3$ (%)	Factor 2 Residual free Ca^{2+} (%) -	Factor 3 Time (min)	Response 1 Y_1: Chl-a removal rate (%)	Response 2 Y_2: COD removal rate (%)
1	12	2	0	60	73.76	73.99
2	8	14	0	60	87.58	68.21
3	2	2	100	60	76.59	84.6
4	16	14	100	60	90.25	42.77
5	6	2	50	10	75.31	79.77
6	9	14	50	10	84.59	65.9
7	7	2	50	110	80.05	90.17
8	13	14	50	110	93.47	71.68
9	17	8	0	10	82.74	79.77
10	10	8	100	10	85.23	50.94
11	4	8	0	110	87.29	63.58
12	11	8	100	110	92.3	76.3
13	14	8	50	60	92.89	87.98
14	1	8	50	60	93.78	84.89
15	5	8	50	60	92.94	90.88
16	3	8	50	60	93.06	86.12
17	15	8	50	60	93.83	90.32

Table S9: Experimental design and results for BBD

151 ## Table S10

Mass fraction of $CaCO_3$(%)	Residual free Ca^{2+}(%)	Time of reaction(min)	Removal-Chl-a (%)		Removel-COD (%)	
			Observed	Predicted	Observed	Predicted
7.51	56	85.35	92.67	93.83	87.23	88.64
7.51	56	85.35	91.98	93.83	86.54	88.64

Table S10: Optimal operating conditions for Chl-a and COD removal efficiency

References

Almomani, F., Bhosale, R.R., 2021. Bio-sorption of toxic metals from industrial wastewater by algae strains spirulina platensis and chlorella vulgaris: Application of isotherm, kinetic models and process optimization. Science of The Total Environment 755, 142654. https://doi.org/10.1016/j.scitotenv.2020.142654

Anderson-Cook, C.M., Borror, C.M., Montgomery, D.C., 2009. Response surface design evaluation and comparison. Journal of Statistical Planning and Inference 139, 629–641. https://doi.org/10.1016/j.jspi.2008.04.004

Grimme, S., Antony, J., Ehrlich, S., Krieg, H., 2010. A consistent and accurateab initioparametrization of density functional dispersion correction (DFT-d) for the 94 elements h-pu. The Journal of Chemical Physics 132. https://doi.org/10.1063/1.3382344

Huang, Y., Wang, Y., Huang, Y., Zhang, L., Ye, F., Wang, J., Shang, J., Liao, Q., 2020. Impact of sediment characteristics on adsorption behavior of typical antibiotics in lake taihu, china. Science of The Total Environment 718, 137329. https://doi.org/10.1016/j.scitotenv.2020.137329

Kresse, G., Furthmüller, J., 1996. Efficient iterative schemes forab initiototal-energy calculations using a plane-wave basis set. Physical Review B 54, 11169–11186. https://doi.org/10.1103/physrevb.54.11169

Monkhorst, H.J., Pack, J.D., 1976. Special points for brillouin-zone integrations. Physical Review B 13, 5188–5192. https://doi.org/10.1103/physrevb.13.5188

Novak, J.T., Brune, D.E., 1985. Inorganic carbon limited growth kinetics of some freshwater algae. Water Research 19, 215–225. https://doi.org/10.1016/0043-1354(85)90203-9

Oss, C.J. van, 1995. Hydrophobicity of biosurfaces — origin, quantitative determination and interaction energies. Colloids and Surfaces B: Biointerfaces 5, 91–110. https://doi.org/10.1016/0927-7765(95)01217-7

Oss, C.J. van, 1993. Acid—base interfacial interactions in aqueous media. Colloids and Sur-

faces A: Physicochemical and Engineering Aspects 78, 1–49. https://doi.org/10.1016/0927-7757(93)80308-2

Perdew, J.P., Burke, K., Ernzerhof, M., 1996. Generalized gradient approximation made simple. Physical Review Letters 77, 3865–3868. https://doi.org/10.1103/physrevlett.77.3865

Veith, J.A., Sposito, G., 1977. On the use of the langmuir equation in the interpretation of "adsorption" phenomena. Soil Science Society of America Journal 41, 697–702. https://doi.org/10.2136/sssaj1977.03615995004100040015x